Band structure and topological phases of $Pb_{1-x-y}Sn_xMn_yTe$ by *ab initio* calculations

A. Łusakowski* and P. Bogusławski
Institute of Physics, Polish Academy of Sciences, Al. Lotników 32/46, 02-668 Warszawa, Poland

T. Story
Institute of Physics, Polish Academy of Sciences, Al. Lotników 32/46, 02-668 Warszawa, Poland
and International Research Centre MagTop, Institute of Physics, Polish Academy of Sciences, Al. Lotników 32/46, 02-668 Warszawa, Poland

(Received 1 October 2020; accepted 4 January 2021; published 12 January 2021)

A change in the composition of the $Pb_{1-x}Sn_xTe$ IV–VI semiconductor or in its lattice parameter can drive a transition from a topologically trivial to a topological crystalline insulator (TCI), crossing a region where the alloy is in the Weyl semimetal phase. Incorporation of the magnetic Mn ions induces strong perturbations of the electronic structure, which act on both orbital and spin variables. Our first principles calculations show that the presence of Mn shifts the TCI and the Weyl region towards higher Sn contents in $Pb_{1-x}Sn_xTe$. When the Mn spin polarization is finite, the spin perturbation, like the orbital part, induces changes in band energies comparable to the bandgap, which widens the Weyl region. The effect opens the possibility of driving transitions between various topological phases of the system by a magnetic field or by spontaneous Mn magnetization. We also propose a new method to calculate topological indices for systems with a finite spin polarization defined based on the concept of the Chern number. These valid topological characteristics enable the identification of the three distinct topological phases of the $Pb_{1-x-y}Sn_xMn_yTe$ alloy.

DOI: 10.1103/PhysRevB.103.045202

I. INTRODUCTION

$Pb_{1-x}Sn_xTe$ and its selenide analog, $Pb_{1-x}Sn_xSe$, are IV–VI narrow-gap semiconductors known to undergo chemical-composition-, pressure-, or temperature-driven band inversion accompanied by a transition from the trivial insulator to the topological crystalline insulator (TCI) phase [1–4]. In contrast to $(Bi, Sb)_2(Te, Se)_3$ chalcogenide topological insulators, in TCIs it is the crystalline (mirror-plane) symmetry, not the time-reversal symmetry, that warrants the existence of Dirac-like states on specific high-symmetry crystal facets of bulk rock-salt crystals. [1,5,6] Experimentally, the TCI surface states were observed by angle- and spin-resolved photoemission electron spectroscopy [2–4,7], scanning tunneling microscopy/spectroscopy [8], and magnetotransport and magneto-optical quantum oscillatory effects [9–11]. The band inversion and topological transition in $Pb_{1-x}Sn_xTe$ were recently analyzed theoretically by ourselves [12] and others [6,13,16,17] using the density functional theory, the tight-binding approximation (TBA), the virtual crystal approximation (VCA), and the method of special quasirandom structures (SQSs) developed [18] for the analysis of substitutional alloys. Confirming the successful basic picture obtained in early VCA calculations [6], the other methods accounted for local chemical disorder, inevitably present in alloys. It was discovered that due to the splitting of the bands induced by locally varying crystal-field symmetry there exists a transition region between the trivial and the TCI phase characterized by a zero-energy gap [12] with a possible Weyl semimetal (WSM) type of energy band arrangement [13].

Other examples of topological transitions, although of a different kind than those considered here, between a TCI and a topological Z2 insulator are proposed in papers by Deng *et al.* [14] and Safaei *et al.* [15].

In the quest for efficient ways of controlling topological insulators and semimetals their alloying with other semiconductor materials proved very promising [5]. Particularly interesting is the alloying of TCIs with magnetic semiconductors, like MnTe and MnSe, thus combing the topological and magnetic properties of materials. Recent developments in the field of topological materials showed rapid progress in ferromagnetic (FM) and antiferromagnetic (AFM) heterostructures expected to exhibit the quantum anomalous Hall effect and topological magnetoelectric effect [5,19,20]. There exist several proposals for controlling topology in TCIs with nonzero magnetization as well as for topological transition from the TCI to the WSM state [21–24].

$Pb_{1-x}Sn_xTe$ with Mn is known as a IV–VI diluted magnetic (semimagnetic) semiconductor exhibiting carrier-induced ferromagnetism driven by the Rudermann-Kittel-Kasuya-Yosida indirect exchange interaction via holes [25,26]. As the solubility limit of Mn in bulk crystals of $Pb_{1-x-y}Sn_xMn_yTe$ is about 12 at%, the ferromagnetic transition temperature observed in the bulk crystals is below 30 K [26–28]. For thin epitaxial layers of the topologically nontrivial terminal alloy, $Sn_{1-x}Mn_xTe$, the solubility appears lower due to the lower temperatures required for epitaxial growth, and the ferromagnetic Curie temperature is below 10 K [24,29]. Importantly, Mn in $Pb_{1-x}Sn_xTe$ substitutes Sn^{2+} or Pb^{2+} ions as the

*lusak@ifpan.edu.pl

isoelectronic Mn^{2+} ion with the configuration $3d^5$ and magnetic moment of 5-Bohr magnetons, as verified by electron paramagnetic resonance studies of both very diluted paramagnetic crystals [30] and more concentrated ferromagnetic ones [31]. The results in Refs. [32–38], as well as the results in Sec. 3 of the Supplemental Material (SM) [39], demonstrate that Mn is not a dopant in $Pb_{1-x}Sn_xTe$. The incorporation of Mn ions into a $Pb_{1-x}Sn_xTe$ crystalline matrix can be viewed as an isoelectronic substitution of Mn^{2+} ions for Sn^{2+} or Pb^{2+} ions with no free carriers generated.

The influence of Mn ions on the band structure of the quaternary system $Pb_{1-x-y}Sn_xMn_yTe$ and corresponding terminal ternary alloys $Pb_{1-x}Mn_xTe$ and $Sn_{1-x}Mn_xTe$ was studied to explain their very good thermoelectric parameters as well as their FM properties. It was found, both theoretically and experimentally, that the key role is played by the band of heavy holes (Σ band) and the position of its top with respect to the top of the highest valence band located at the L point in the Brillouin zone (BZ) [32–38]. A good agreement was achieved between theoretical predictions and optical and thermoelectric data for the topologically trivial $Pb_{1-x}Mn_xTe$ alloy: with increasing Mn content the main gap at the L point increases while the energy separation between the L and the Σ bands decreases [32–34]. Theoretical studies of the band structure of the TCI $Sn_{1-x}Mn_xTe$ agreed on the decreasing energy separation of the L and Σ bands but provided conflicting predictions for the main gap at the L point, finding either its increase [35–37] or its decrease [38] with increasing Mn content. The band structure of $Pb_{1-x-y}Sn_xMn_yTe$ in the band inversion region was not studied theoretically with *ab initio* methods. In the early model analysis of the temperature, composition, and carrier concentration dependence of the thermoelectric power of $Pb_{1-x-y}Sn_xMn_yTe$ it was assumed that the main gap at the L point increases with increasing Mn content [40], as typically observed in known II–VI and IV–VI diluted magnetic (semimagnetic) semiconductor materials.

In the present work, we employ first principles calculations to study the influence of Mn ions on the electronic structure of $Pb_{1-x-y}Sn_xMn_yTe$. Incorporation of magnetic Mn ions into such crystals, apart from the changes in chemical composition and local crystal symmetry, leads in general to breaking of the time-reversal symmetry. A finite spin polarization of the Mn sublattice induces large spin splittings of the band states, which can be comparable to the bandgap energy.

By analyzing the band structure, topological indices, and charges, as well as the Weyl's nodes we demonstrate how changes in the chemical composition or in the lattice parameter (by pressure or strain) induce a transition from the trivial to the TCI phase of $Pb_{1-x-y}Sn_xMn_yTe$. Typically, the transition passes through an intermediate region characterized by a zero-energy gap, corresponding to the WSM phase. Importantly, we predict that the transition from the trivial to the Weyl phase can be driven by the magnetic field or by spontaneous magnetization.

The response of a band extremum to the perturbation induced by Mn depends on its symmetry, and it is different for the states derived from the L_6^+- and the L_6^--band extrema of PbTe and SnTe. This holds for both the spin and the orbital perturbation. We trace this effect to the symmetry-dependent hybridization between the p(Te) and the s(Mn) and d(Mn) orbitals.

The presence of the Mn ions leads to an increase in the bandgap in the trivial region but to a decrease in the absolute value of the inverted gap in the TCI phase. This result is in agreement with experimental observations available for the trivial phase, e.g., in $Pb_{1-x}Mn_xTe$ [41]. The calculated impact of Mn on the inverted gap in the TCI phase is particularly relevant. Indeed, in this case analysis of experimental data (see, e.g., Ref. [40]) is obscured by contradictory theoretical predictions [35–37], and the conclusions depend on the specific band structure models adopted in the interpretation.

II. TECHNICAL DETAILS OF CALCULATIONS

A. Modeling of disordered $Pb_{1-x-y}Sn_xMn_yTe$ crystals

Infinite $Pb_{1-x-y}Sn_xMn_yTe$ random mixed crystals are modeled by $2 \times 2 \times 2$ supercells containing 64 atoms: 32 Te anions and 32 Pb, Sn, or Mn cations. In the following, instead of $Pb_{1-x-y}Sn_xMn_yTe$ with the specified x and y we often use the notation $Pb_kSn_lMn_mTe_{32}$, where k, l, and m ($k + l + m = 32$) are the numbers of Pb, Sn, and Mn atoms in the 64-atom supercell, respectively. The most important problem is the choice of the spatial distribution of cations in the supercell, because, as we showed in Ref. [12] for $Pb_{1-x}Sn_xTe$, the band structure and, in particular, the energy gap E_{gap} strongly depend on the cation configuration.

To solve this problem, we applied the SQS approach [18]. The aim of this approach is to find positions of different cations in the supercell such that their distribution resembles a random distribution of cations in the infinite alloy as much as possible for several coordination spheres. However, for three cations in the supercell, Pb, Sn, and Mn, the number of their possible configurations is much larger than in the case of Pb and Sn only, thus the probability of finding the best possible SQSs is much lower. In spite of this, as shown in the following, although the calculated dependencies of energy gaps on the Sn concentrations are not perfectly smooth, general trends can be easily resolved. This issue is discussed in some detail in the Supplemental Material, Sec. 2 [39], where we show the results obtained for different relative positions of Mn atoms (Fig. SM2 [39]) and for random distributions of cations in the supercell (Fig. SM3 [39]). Although the results differ somewhat from those using the SQS approach, neither the qualitative picture nor the conclusions change.

For a given distribution of cations, the starting point of our analysis is the density functional theory calculations performed with the open-source OpenMX package [42]. The calculations were done using the local density approximations with the Ceperly-Alder [43] exchange-correlation functional. For Sn and Mn we used pseudopotentials distributed with OpenMX (version 2013), and for Pb and Te we used pseudopotentials with four and six valence electrons, respectively, generated previously using the program ADPACK distributed with OpenMX. All the input parameters for calculations of pseudopotentials for Pb and Te are described in Ref. [32].

To improve the accuracy of calculations based on approximate density functionals, the $+U$ corrections are often included [44]. We performed test calculations with $U(\mathrm{Mn}) =$

1.5 eV. This value was assessed for Mn in ZnO [45]. The results are presented in Sec. 3 of the Supplemental Material [39]. They demonstrate that the changes of all properties studied here are practically not affected by using $U(\mathrm{Mn}) = 1.5$ eV instead of the $U = 0$ assumed in our calculations. One can also observe that the d(Mn) states form a peak in the density of states about 4 eV below the VBM, somewhat sharper for $U(\mathrm{Mn}) = 1.5$ eV than for $U(\mathrm{Mn}) = 0$. Nevertheless, the peak energy is in excellent agreement with the resonant photoemission measurements for $Sn_{1-x}Mn_xTe$ [46] but a detailed comparison with experiment is beyond the scope of this work.

In the calculations we assume the experimental dependence of the lattice parameter on the chemical composition [47]:

$$a = 6.460 - 0.145x - 0.558y \text{ Å}. \tag{1}$$

The experimental equilibrium Mn-Te bond length, $d_{\text{Mn-Te}} \approx 2.96$ Å, is much smaller than $d_{\text{Pb-Te}} \approx 3.23$ Å and $d_{\text{Sn-Te}} \approx 3.16$ Å [48]. Consequently, the ions in the alloy do not occupy perfect NaCl lattice sites, and the internal distortions are of importance when considering the alloy bandgap. We show below that the hybridization between $3d$(Mn), $4s$(Mn), and $5p$(Te) orbitals has an important influence on the energy gap. This effect depends on the distance between Mn and Te, making the geometry optimization necessary.

The energy gaps presented in the figures are the minimal direct energy gaps in the [111] direction in the three-dimensional BZ. However, one should keep in mind that, contrary to PbTe or SnTe, due to the lack of O_h local symmetry in most of the considered systems the smallest energy gaps are not, in general, placed in this direction (see the next section for an example).

The calculations are mostly done for systems containing even numbers of Mn ions in the supercell. With this choice one can study the impact of Mn doping on $Pb_{1-x}Sn_xTe$ in the paramagnetic case, by assuming AFM spin configurations with the vanishing total spin, and separate the effects of spin polarization, modeled by assuming FM spin configurations. In the latter case, the valence and conduction bands are spin-split, which in turn significantly affects the energy gaps, particularly when they are very small. Both situations are accessible experimentally, since the Curie temperature in the p-doped tin tellurides is of the order of 10 K.

B. Calculations of topological indices

The OpenMX package enables us to obtain TBA parameters for the TBA Hamiltonian. Using these parameters we calculate the necessary topological indices: the Chern numbers, the spin Chern numbers, and the numbers C_{s+} and C_{s-} [49]. The method of calculation of C_{s+} and C_{s-} is described in Ref. [12]. In short, the idea is to divide the valence band states for every $\boldsymbol{k}$ in the BZ into two sets, $P_+(\boldsymbol{k})$ and $P_-(\boldsymbol{k})$. In $P_+(\boldsymbol{k})$ [$P_-(\boldsymbol{k})$] there are states with positive [negative] average spin. Taking the sums over $\boldsymbol{k}$ we obtain two vector bundles, $P_+ = \oplus_{\boldsymbol{k}} P_+(\boldsymbol{k})$ and $P_- = \oplus_{\boldsymbol{k}} P_-(\boldsymbol{k})$. Calculating the Chern numbers for these bundles we obtain C_{s+} and C_{s-}. The spin Chern number $\mathrm{SCN} = (C_{s+} - C_{s-})/2$. The method of calculation of $C_{s\pm}$ is based on the approach proposed by Fukui *et al.* [50].

The microscopic Hamiltonian, i.e., the Pauli-Schrödinger Hamiltonian for electrons in $Pb_{1-x-y}Sn_xMn_yTe$, is time reversal invariant. However, after the density functional theory calculations the time-reversal invariance is broken. The resulting spins of ions are finite and consequently the resulting TBA Hamiltonians have no time-reversal symmetry. This feature was directly checked in a number of cases. Therefore, the general theorem that the Chern number calculated for a given two-dimensional plane in the three-dimensional BZ should be 0 is not valid.

The BZ of our supercells is a cube. In the calculations of topological indices we use the (001) plane crossing the $\boldsymbol{k} = (0, 0, 0)$ Γ point. This point corresponds to the L points of the unfolded BZ, and the main energy gap is situated at Γ or in its close vicinity.

The procedure for calculation of spin Chern numbers described previously [12] can be applied directly to the systems without magnetic ions or those containing an even number of magnetic ions in the supercell, arranged in such a way that their total magnetic moment vanishes. Then the dimensions $n_\pm(\boldsymbol{k})$ of $P_\pm(\boldsymbol{k})$ are equal, $n_+(\boldsymbol{k}) = n_-(\boldsymbol{k})$. In the case where the total spin of the system is nonzero the procedure must be modified. In general, $n_+(\boldsymbol{k}) \equiv n_+$ and $n_+(\boldsymbol{k}) \equiv n_-$ are independent of $\boldsymbol{k}$, and they are related by $n_+(\boldsymbol{k}) = n_-(\boldsymbol{k}) + N_S$, where $N_S = 5(N_{\mathrm{Mn}\uparrow} - N_{\mathrm{Mn}\downarrow})$; exceptions are discussed below. Here $N_{\mathrm{Mn}\uparrow}$ and $N_{\mathrm{Mn}\downarrow}$ are the numbers of Mn atoms in the supercell with spin-up and -down, respectively, and the factor 5 is related to the number of unpaired spins on the $3d$(Mn) shell. Thus,

$$n_- = (n_{\mathrm{val}} - N_S)/2, \quad n_+ = (n_{\mathrm{val}} + N_S)/2, \tag{2}$$

where n_{val} is the number of occupied states. This is related to the exchange polarization of the bands due to nonvanishing net magnetization caused by Mn ions. Next, we divide the valence states into two subspaces and calculate the Chern numbers C_{s+} and C_{s-}.

This procedure was applied successfully in a vast majority of cases, however, for completeness, one should mention possible problems. Sometimes, the calculated C_{s+} and C_{s-} are noninteger. For example, for $Pb_{31-n}Sn_nMn_1Te_{32}$ meaningful results (integer $C_{s\pm}$) are obtained only for trivial and nontrivial regions, $n \leqslant 9$ and $n \geqslant 17$, respectively. In the transition region $10 \leqslant n \leqslant 16$, where the values of the energy gaps are nearly 0, the procedure fails. This is related to the fact that in such cases there are a few points in the two-dimensional plane of the BZ where the numbers of states with positive and negative average spins are not equal to n_+ and n_- as in Eq. (2) but equal to $n_+ + 1$ and $n_- - 1$, respectively. Thus it is impossible to build two vector bundles P_+ and P_- of dimensions n_+ and n_-, respectively, and to calculate the corresponding C_{s+} and C_{s-}. The reason for these problems is the practically vanishing E_{gap}. A detailed analysis shows that in the transition region the system is in the Weyl semimetal phase, and sometimes the Weyl's nodes are on the plane in $\boldsymbol{k}$ space used to calculate C_{s+} and C_{s-}. Of course, for systems with $E_{\mathrm{gap}} = 0$ the calculations of Chern numbers do not make sense. The example of $Pb_{15}Sn_{16}Mn_1Te_{32}$ is discussed in the next section.

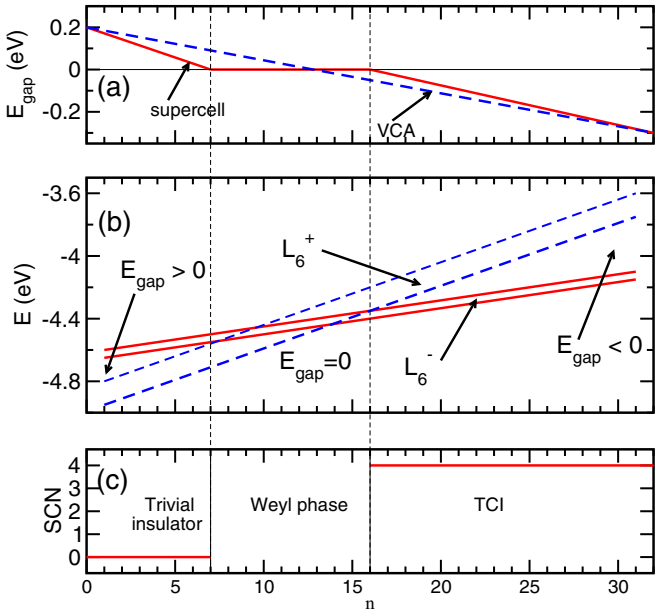

FIG. 1. Schematic of the composition dependence of the relevant physical parameters of the $Pb_{1-x}Sn_xTe$ alloy. n is the number of Sn atoms in the $Pb_{32-n}Sn_nTe_{32}$ supercell. (a) Energy gap calculated within the supercell method (solid line) and with the VCA (dashed line). (b) Splittings of the energy levels at the Γ point for the supercell BZ. The energies of L_6^-- and L_6^+-derived states are between the solid red and the dashed blue lines, respectively. (c) Spin Chern number for the trivial and the TCI phase separated by the Weyl semimetal phase.

C. Calculations for the Weyl semimetal region

Analysis of the Weyl semimetal phase is not an easy numerical task because the zero-energy gap points are grouped in the close vicinity of the Γ point in the supercell BZ. In the studied cases, all the Weyl nodes are contained in a cube of dimension 0.02 $Å^{-1}$. In a few cases we identified the points in the BZ where $E_{gap} = 0$. However, in most cases we applied a much faster, although less accurate method. Namely, a cube with the edge of 0.02 $Å^{-1}$ was divided into 1000 smaller cubes with edges of 0.002 $Å^{-1}$. Next, for all small cubes we calculated the Berry flux through their faces. Of course, in this procedure we miss the cases where a pair of Weyl nodes of opposite charges is present inside a small cube.

III. RESULTS AND DISCUSSION

We begin with a brief summary of the main features characterizing the electronic structure of $Pb_{1-x}Sn_xTe$ [12] without Mn ions. Energy bands of PbTe and SnTe are presented in Fig. SM1 [39]. Figure 1 schematically shows the composition dependence of the bandgap, together with the relevant energies of the valence and conduction bands at the Γ point of the supercell BZ and the topological indices.

With increasing Sn content, E_{gap} changes character from positive in PbTe to negative in SnTe [Fig. 1(a)], driving the system from topologically trivial to a TCI, which is also reflected in the nonvanishing spin Chern numbers in the Sn-rich $Pb_{1-x}Sn_xTe$. Qualitatively different characters of the transition are obtained in the VCA and in the supercell method used in this paper.

In the VCA, the chemical disorder of an alloy is absent, and the system retains both the O_h point symmetry and the translational symmetry of the rock salt structure. As a result, the transition between topologically trivial and nontrivial phases is sharp and takes place at a well-defined critical composition. In the supercell method, the alloy is simulated by the repeated supercells. The L points of the PbTe (or SnTe) BZ are folded to the Γ point of our 64-atom supercell BZ. After the folding, both the L_6^+- and the L_6^--derived bands of pure PbTe are eightfold degenerate. These degeneracies are lifted in the presence of two types of cations because of the different chemical nature of Pb and Sn and because of the disorder in their spatial distribution. This splitting is schematically shown in Fig. 1(b). The magnitude of splittings and possible final degeneracies (e.g., double degeneracies in systems with inversion symmetry discussed below) depend on the actual distribution of Pb and Sn in the supercell. Consequently, in the supercell approach the trivial-TCI transition is smeared, there is a relatively wide composition window in which the bandgap between occupied and unoccupied states vanishes, and the system is in the WSM phase [13], where topological indices are in general not defined.

The energy of the L_6^-- relative to the L_6^+-band extremum can also be reduced by application of the hydrostatic pressure. This closes the positive gap of PbTe, opens the negative gap of SnTe, and can drive the pressure-induced transition from the trivial to the TCI phase in $Pb_{1-x}Sn_xTe$. Again, the splitting of the energy levels leads to a smeared character of the transition, which proceeds through the Weyl phase (see Ref. [13] for details). In the VCA the transition is sharp, and the WSM phase is absent. Remarkably, the existence of a semimetal region in $Pb_{1-x}Sn_xTe$ was proposed based on recent experimental studies of temperature and composition dependence of conductivity [51].

A. Comparison of $Pb_{30}Sn_2Te_{32}$ and $Pb_{30}Mn_2Te_{32}$

Mn ions in $Pb_{1-x}Sn_xTe$ are magnetic and assume the high-spin state $S = 5/2$. The substitution of Mn for a cation introduces a perturbation acting on both the orbital and the spin variables, which in the following are referred to as the chemical and the spin part of perturbation, respectively. Both effects are analyzed here. The spin perturbation affects the band structure only when the Mn sublattice is spin-polarized. Accordingly, we assume a finite spin polarization of Mn (present in the FM phase or induced by a weak magnetic field), but its influence on the orbital motion (including the Landau quantization) is neglected, because it requires a different approach to the band structure calculations, such as the effective mass model.

We first neglect the spin perturbation and compare the impact of doping PbTe with Sn and Mn. The comparison reveals the main features also present in the remaining cases. The results, obtained for a 64-atom PbTe supercell containing two Sn ions and one containing two Mn ions with antiparallel spins, are presented in Fig. 2. The figure shows the effect of hydrostatic pressure (monitored by the decrease in a) on the electronic structure. The positions of Sn and Mn atoms in

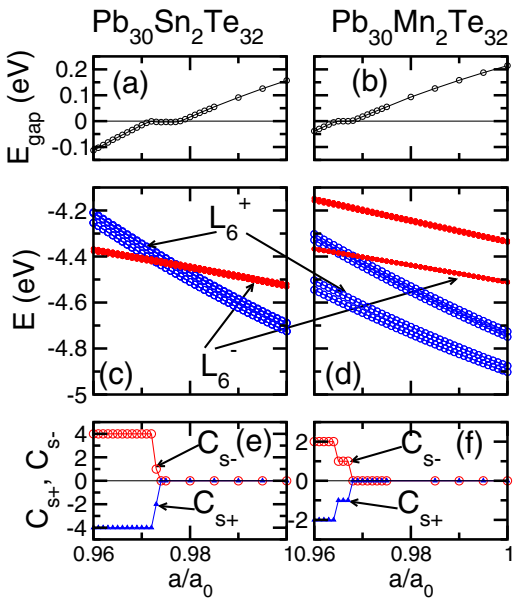

FIG. 2. Dependence on the lattice parameter a of (a, b) the energy gap, (c, d) splitting of the L_6^+- and L_6^--derived levels at the Γ point of the supercell BZ, and (e, f) the Chern numbers C_{s+}, C_{s-}. Left panels, $Pb_{30}Sn_2Te_{32}$; right panels, $Pb_{30}Mn_2Te_{32}$. a_0 is the equilibrium lattice parameter of PbTe.

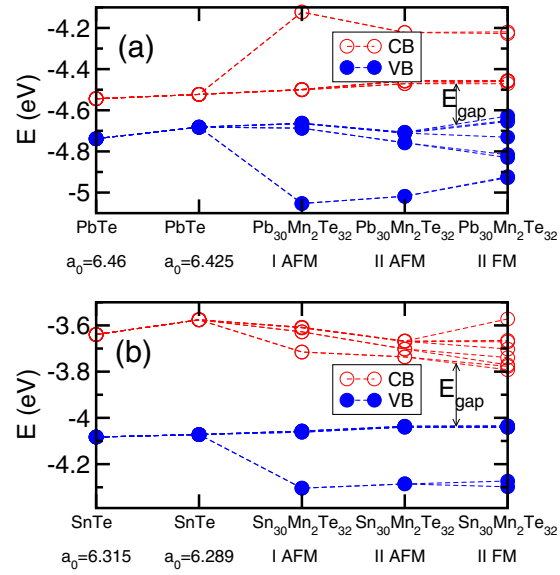

FIG. 3. Energy levels of the highest valence and the lowest conduction bands at the Γ point of the supercell BZ for (a) PbTe and (b) SnTe with two Mn ions. The consecutive steps correspond to the adjustment of the lattice parameter, the introduction of Mn with antiparallel spins without (I) and with (II) lattice relaxation, and the FM spin arrangement.

the supercells are the same, and the internal relaxations are neglected.

From Figs. 2(a) and 2(b) it follows that the incorporation of Mn ions into PbTe at equilibrium $a = a_0 = 6.46$ Å leads to an increase in the bandgap from 0.20 eV for PbTe to 0.214 eV for $Pb_{30}Mn_2Te_{32}$, while the incorporation of Sn decreases E_{gap} to 0.16 eV in $Pb_{30}Sn_2Te_{32}$ in accord with measurements [52,53]. Considering the pressure dependence of the bandgap we find that for both $Pb_{30}Sn_2Te_{32}$ and $Pb_{30}Mn_2Te_{32}$, E_{gap} decreases with the decreasing lattice constant a (i.e., with the increasing hydrostatic pressure) and eventually changes sign to negative, again in agreement with experiment [41,52–54].

The pressure dependence of E_{gap} shows regions where the bandgap practically vanishes, and both systems are in the WSM phase. This effect was pointed out above and is related to the alloy broadening, i.e., to the splitting of energy bands in mixed crystals. The splitting is shown in some detail in Figs. 2(c) and 2(d). At the Γ point of our 64-atom supercell BZ, the L_6^+- as well as the L_6^--derived bands of PbTe are eightfold degenerate. These degeneracies are lifted in the presence of the Sn or Mn ions. Comparing the results for $Pb_{30}Sn_2Te_{32}$ and $Pb_{30}Mn_2Te_{32}$ we see that the level splittings, and thus the alloy broadening of the energy spectrum, are much larger in the latter case. This is because the substitution of Pb by a group II Mn ion generates a stronger crystal and electronic perturbation than the substitution of Pb by the isoelectronic Sn.

Finally, Figs. 2(e) and 2(f) show the topological indices for the two alloys. The sign of the energy gaps in Figs. 2(a) and 2(b) is determined by zero or nonzero values of the spin Chern number. Again, in agreement with Figs. 2(c) and 2(d), the Weyl region between the TCI and the trivial phases is broader in $Pb_{30}Mn_2Te_{32}$, although it is less clear in Figs. 2(a) and 2(b).

B. Influence of Mn on the band structure of $Pb_{30}Mn_2Te_{32}$ and $Sn_{30}Mn_2Te_{32}$

The influence of Mn ions on the band structure of PbTe and SnTe is analyzed in Fig. 3, which shows the energy position of the eight highest valence bands and the eight lowest conduction bands. As before, we use supercells with the lattice parameters taken according to Eq. (1) and containing two Mn ions. The Mn ions are placed at (0, 0, 0) and a_0(1, 1, 1) in a perfect rock salt lattice neglecting the internal distortions. Thus, the Mn ions form a cubic body centered lattice, and the system has O_h symmetry. With this choice the wave functions are either even or odd with respect to inversion (like the wave functions of the L_6-band extrema in PbTe and SnTe), which makes the analysis more transparent. We mention that the calculated bandgaps differ from those obtained with the SQS method, which reflects the dependence of E_{gap} on the Mn distribution. More details are provided in Sec. 2 of the SM [39]. The choice of supercells with an even number of Mn ions allows for separation of the effects induced by the chemical and the spin perturbation, which is achieved by comparing the FM and AFM spin configurations.

The final band structure of both systems is achieved in four steps. In the first step, the pure compound is dilated or compressed to the appropriate lattice constant. In the second step, Mn ions are introduced to the supercell in the AFM spin configuration, but the atoms are not allowed to relax, which is denoted configuration I. We see that for both systems the Mn chemical perturbation induces splittings of the eightfold degenerate band extrema by 0.1–0.3 eV, which is comparable to E_{gap} of the PbTe and SnTe hosts.

In the third step, atoms relax to configuration II, in which the nearest Te neighbors are moved towards the Mn ions along

the bond directions, so that the Mn-Te bonds are reduced from 3.23 to 2.95 Å. The latter value is equal to that obtained after the geometry optimization and, in the case of $Sn_{1-x}Mn_xTe$, is very close to the experimental one [48]. This effect leads to small changes in band energies. In the last step we assume the FM spin arrangement. Inclusion of the spin polarization reduces E_{gap}. In both PbTe and SnTe, the spin splittings are large, showing that the spin and the chemical perturbation are equally important and can be comparable to the bandgap.

Interestingly, as follows from Fig. 3, the response to the Mn perturbation depends on the band symmetry. In particular, the spin splittings are considerably more pronounced in the case of the bands derived from L_6^+ than those derived from the L_6^--band extrema, independent of the host and of the valence or conduction band character. We relate this result to the atomic orbital composition of the corresponding wave functions. In the case of $Pb_{30}Mn_2Te_{32}$, the wave functions of the VBM are even with respect to the inversion symmetry operation. They contain contributions from the $3d$(Mn) orbitals, and these contributions are larger for configuration II than for configuration I. This is due to the stronger hybridization of $3d$(Mn) with p(Te) after lattice relaxation, when the Mn-Te bonds are shorter. The wave functions of the L_6^--derived conduction levels are odd with respect to the inversion and practically do not contain Mn orbitals and do not respond to the presence of Mn. The situation is different in $Sn_{30}Mn_2Te_{32}$. The wave functions of the three highest valence levels shown in Fig. 3 are odd with respect to inversion and contain contributions from neither the $4s$(Mn) nor the $3d$(Mn) orbitals, while the lowest level is even and contains the contribution from $4s$(Mn) orbitals.

C. Supercells with zero, two, or four manganese ions

In this section we analyze the dependence of the energy gap and topological properties of $Pb_{1-x-y}Sn_xMn_yTe$ on the Sn concentration. The impact of Mn is revealed by comparing three cases—that with no Mn, $y = 0$, that with $y = 0.0625$, and that with $y = 0.125$—which correspond to 0, 2, and 4 Mn atoms at the cation sites of a 64-atom supercell, respectively. We begin with the antiferromagnetic configuration of Mn spins. In Fig. 4 we show E_{gap} and the corresponding topological indices as a function of the Sn concentration. The increase in E_{gap} with increasing Mn content in PbTe was analyzed above. As we pointed out, doping PbTe with Mn lowers the energy of the L_6^+ band relative to the L_6^- band, thus increasing the bandgap. In SnTe this effect takes place as well, but in this case it decreases the inverted E_{gap}. As follows from Fig. 4, this effect of Mn persists also in the $Pb_{1-x-y}Sn_xMn_yTe$ alloy over the whole composition range.

While the decrease in energy of L_6^+ relative to L_6^- induced by two and four Mn ions in the supercells is clear for all Sn concentrations, it is not always possible to distinguish the results for two and four Mn ions. This problem stems from the fact that the differences in band energies, in particular, the bandgap itself, are smaller than the fluctuations inherent to our approach. Indeed, they could be eliminated by averaging over a substantially larger number of atomic configurations in the supercells. Apparently, in this specific case, the SQS approximation is not accurate enough.

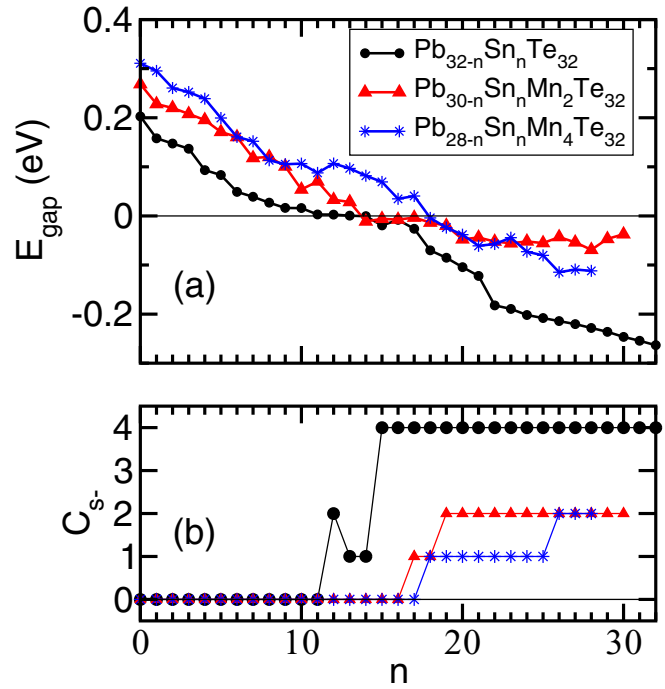

FIG. 4. Dependence on the number of Sn ions in the supercell of (a) the energy gaps and (b) the spin Chern number C_{s-} for $Pb_{32-n}Sn_nTe_{32}$ (circles), $Pb_{30-n}Sn_nMn_2Te_{32}$ (triangles), and $Pb_{28-n}Sn_nMn_4Te_{32}$ (asterisks).

In spite of that problem, two qualitative effects should be noted. First, we find that as a result of the Mn-induced change in E_{gap} in $Pb_{1-x-y}Sn_xMn_yTe$ the trivial-to-nontrivial transition region is shifted to higher concentrations of Sn. Our calculations indicate that for $Pb_{1-x}Sn_xTe$ the energy gap vanishes for $x \approx 0.35$, which corresponds quite well with the experimental value $x \approx 0.4$. For $Pb_{1-x-y}Sn_xMn_yTe$ with $y \approx 0.06$, $E_{gap} = 0$ for a higher $x \approx 0.5$, but the precise experimental value is not known.

Second, since adding Mn enhances alloy broadening, one would expect that the region of the Weyl phase is wider in $Pb_{1-x-y}Sn_xMn_yTe$ than in $Pb_{1-x}Sn_xTe$. Paradoxically, the calculated $E_{gap}(x)$ dependence exhibits an opposite effect, and in the case of four Mn ions in the supercell the Weyl phase is practically absent. This effect is ascribed to the fact that the splittings of both the VBM and the CBM significantly increase with increasing Mn concentration. This is illustrated in Fig. 5, which presents the energies of the eight highest valence states and the eight lowest conduction states at Γ as a function of the Sn concentration in $Pb_{1-x}Sn_xTe$ with zero, two, and four Mn ions in the supercell. Indeed, in the case of $Pb_{1-x}Sn_xTe$ the spread is the smallest, and the levels are almost degenerate, which is reflected in the wide composition window of the Weyl phase. On the other hand, in the case of four Mn ions the spread of the levels is substantial, their energies are well resolved, and the transition is sharp.

The strong chemical disorder may also explain why the Weyl phase is usually not observed in experiments, with the exception of one work [55], in which crystals with extremely low carrier concentrations were used. In actual alloys, apart from the chemical disorder, there are also native defects,

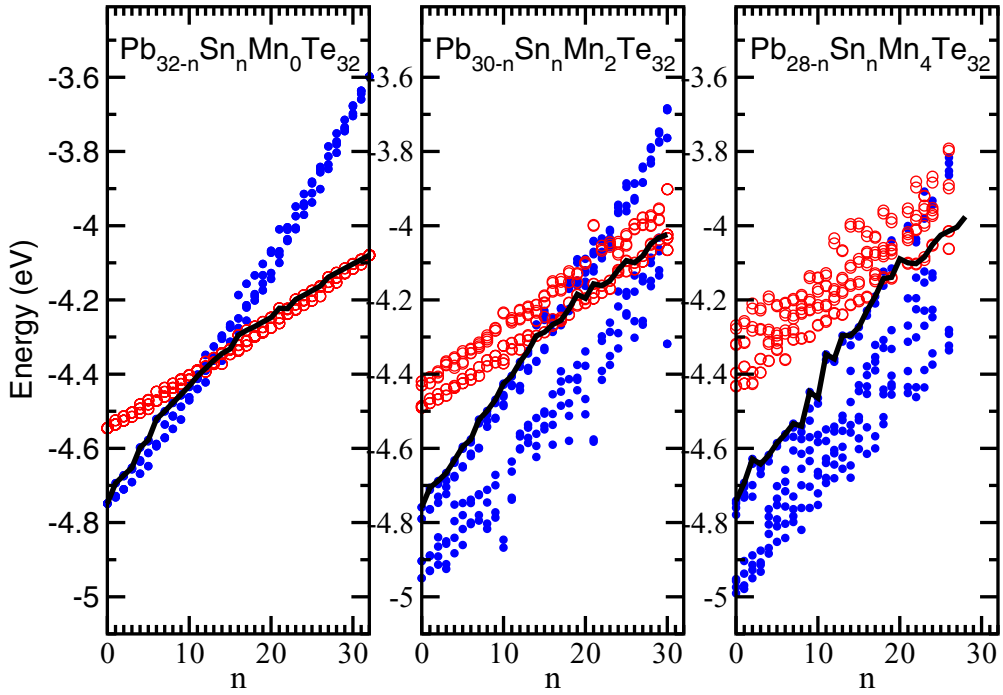

FIG. 5. Dependencies of 16 energy levels nearest to the Fermi energy at the Γ point of the supercell BZ for different Mn concentrations. Filled symbols represent the levels with the wave functions dominated by 5p(Te) orbitals (L_6^+-derived states), and open symbols correspond to those dominated by cation p orbitals (L_6^--derived states). Thick black lines show the energy positions of the VBM.

mostly vacancies, which increase the disorder and can lead to larger band splittings.

We now turn to the impact of spin polarization on the energy levels in $Pb_{1-x-y}Sn_xMn_yTe$. It is shown in detail in Fig. 3 for PbTe and SnTe with two Mn ions constituting the BCC lattice. Figure 6 compares the composition dependence of the bandgap for different spin configurations for $Pb_{1-x-y}Sn_xMn_yTe$ containing two and four manganese atoms in the supercells. In the FM configuration, the spin splittings of the VBM and CBM induce a considerable reduction in the absolute value of E_{gap}. As a consequence of spin polarization, in the case of alloys with two Mn ions the Weyl region characterized by $E_{gap} = 0$ is three times wider than that in the AFM case. In the case of four Mn in the supercells, the effect is even more dramatic, since E_{gap} vanishes for all compositions with $x > 0.25$. Indeed, this is in sharp contrast with the very narrow composition window calculated in the absence of spin polarization. These results are in qualitative agreement with those in Ref. [21], which also finds that the width of the Weyl region increases with the spin polarization of magnetic ions.

The above results, together with those for the supercells with three spin-up and one spin-down Mn ions, allow for a few quasiquantitative conclusions. Namely, in the case of PbTe, incorporation of two Mn ions in the AFM state increases E_{gap} by 0.03 eV, while their spin polarization lowers E_{gap} by about the same amount. Thus, the presence of two Mn ions in the FM configuration leaves the bandgap unchanged, which illustrates well our earlier conclusion that the chemical and the spin perturbations are equally important. The analogous result holds in the case of four Mn ions in supercells. The results for the intermediate case of four Mn ions, three spin-up and one spin-down, are fully consistent with this picture.

In previous works, the trivial-to-TCI phase transition was induced either by a change in composition of $Pb_{1-x}Sn_xTe$ or

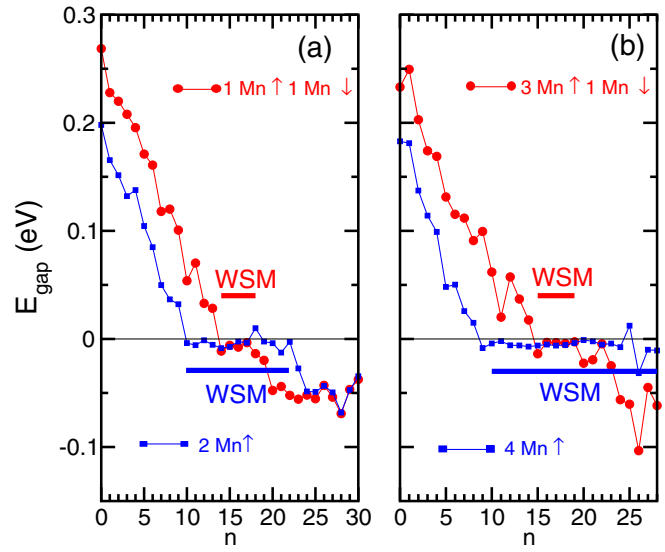

FIG. 6. Dependence of the energy gap on the spin polarization for supercells containing (a) two Mn and (b) four Mn atoms. Orientations of Mn spins and spin configurations are shown by arrows. Thick horizontal lines denote the regions of the Weyl semimetal phase (WSM) where the number of Weyl nodes is nonzero. n is the number of Sn atoms in the supercell.

TABLE I. Weyl points ($k_{x,y,z}$) in the BZ of a 64-atom supercell, calculated energy gaps (E_g), corresponding topological charges (TCs), and energy positions of the Weyl's nodes for $Pb_{15}Sn_{16}Mn_1Te_{32}$.

k_x (Å^{-1})	k_y (Å^{-1})	k_z (Å^{-1})	E_g (eV)	TC	E_{val} (eV)
0.003539	0.001528	0.000406	6.41×10^{-7}	−1	−4.2753
0.000002	−0.005624	0.002274	6.75×10^{-7}	1	−4.2780
−0.002882	0.002512	−0.003221	3.70×10^{-7}	1	−4.2761
0.000131	−0.005761	−0.002160	1.07×10^{-6}	−1	−4.2782

by hydrostatic pressure. The results in Figs. 4 and 6 point to the very interesting possibility of driving the transition by applying a magnetic field. Indeed, in the case of $Pb_{1-x}Sn_xTe$ with composition $x = 0.25$ with four Mn ions, $E_{gap} = 0.1$ eV in the paramagnetic case, i.e., in the AFM configuration, but vanishes in the FM configuration. Such a scenario is also discussed in Ref. [21].

D. The Weyl semimetal phase

A detailed characterization of the Weyl semimetal phase is provided in Table I, where we list the positions of Weyl's nodes in the $\boldsymbol{k}$ space, the corresponding energy gaps, the topological charges, and the energies of the nodes for $Pb_{15}Sn_{16}Mn_1Te_{32}$. The vanishing E_{gap} makes it impossible to calculate the topological indices, as discussed in Sec. II.

As shown in Fig. 7, the analysis of Weyl's nodes helps to define more precisely the transition region between the trivial and the TCI phase. In the case of four Mn ions in the supercell we find only one Sn concentration, $n = 18$, for which the number of Weyl's nodes is nonzero. This confirms the fact that for higher concentrations of Mn the Weyl region is very narrow or is just absent.

Finally, as an additional example, we analyzed the number of Weyl's nodes as a function of the lattice parameter for $Pb_{1-x-y}Sn_xMn_yTe$ containing one Mn ion in the supercell.

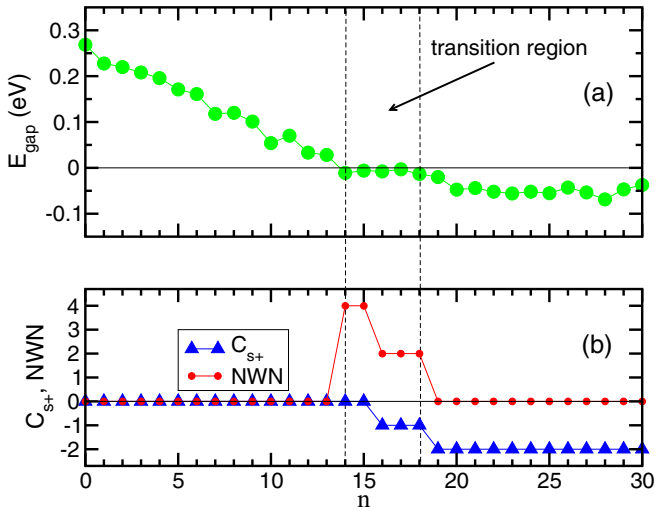

FIG. 7. (a) Energy gaps and (b) topological indices C_{s+} and number of Weyl nodes (NWNs) for two Mn ions set up antiferromagnetically in $Pb_{30-n}Sn_nMn_2Te_{32}$.

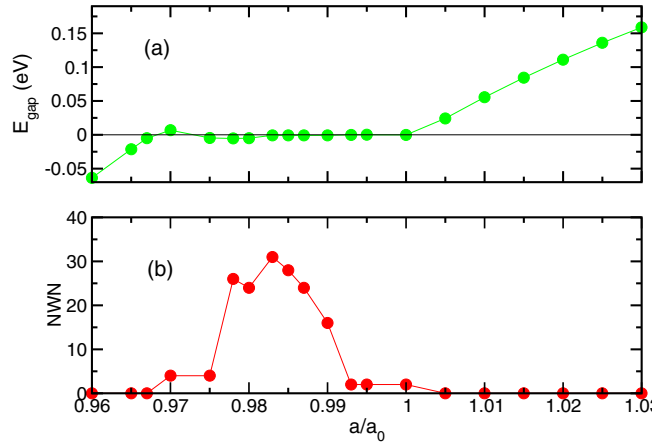

FIG. 8. (a) Energy gap and (b) number of Weyl nodes (NWNs) for $Pb_{23}Sn_8Mn_1Te_{32}$ as a function of the lattice parameter. a_0 is the equilibrium lattice parameter of PbTe.

The results are presented in Fig. 8. They show that the number of Weyl's nodes provides a precise measure of the width of the Weyl region.

IV. CONCLUSIONS

With increasing Sn content in the $Pb_{1-x}Sn_xTe$ alloy, a transition from the topologically trivial to the nontrivial topological crystalline insulator phase takes place. The transition is smeared, because there is a wide composition window, in which the alloy has a zero bandgap and remains in the Weyl semimetal phase. The calculated critical Sn concentration corresponding to the onset of the transition of $Pb_{1-x}Sn_xTe$ to the Weyl phase, $x = 0.3$, is reasonably close to that observed experimentally. The Weyl phase extends from 0.3 to 0.5, and for higher x the alloy assumes the TCI phase.

Using *ab initio* calculations we investigate the consequences of alloying $Pb_{1-x}Sn_xTe$ with Mn. Group II Mn is chemically different from the Pb and Sn group IV cations, and thus it introduces a strong chemical perturbation of the $Pb_{1-x}Sn_xTe$ electronic structure. Next, since Mn in the IV–VI compounds is in the high-spin state, perturbation acting on spin variables of band carriers is present when the macroscopic spin polarization of Mn ions is finite. The main conclusions are as follows.

(1) At higher temperatures, the system is paramagnetic with vanishing spin polarization. In this case, the incorporation of Mn ions into $Pb_{1-x}Sn_xTe$ leads to an increase in E_{gap} on the PbTe side and its decrease on the SnTe side, which modifies the composition window of the Weyl phase. At sufficiently low temperatures the Mn system in $Pb_{1-x-y}Sn_xMn_yTe$ can be spin-polarized, and the spin splittings of the CBM and the VBM are comparable to the bandgap, again considerably widening the Weyl region. For example, in the presence of $y \approx 0.06$ Mn, the Weyl region shifts from $0.3 < x < 0.5$ in $Pb_{1-x}Sn_xTe$ to $0.5 < x < 0.8$. When the Mn ions are fully spin-polarized, the Weyl region extends from $y = 0.5$ to $y = 1.0$.

(2) The strong impact of the spin polarization on the energy bands opens the interesting possibility of inducing a

transition from the trivial to the Weyl phase by a magnetic field or by spontaneous magnetization. The effect is expected to occur for $x > 0.35$.

(3) $Pb_{1-x-y}Sn_xMn_yTe$ alloys can be characterized by topological indices, which are based on the concept of the Chern number. If the total spin polarization of the Mn ions vanishes, the spin Chern number constitutes the appropriate topological index. In other cases, the alloy can be characterized by two indices, C_{s+} and C_{s-}. The dependencies of E_{gap} on the Sn content or on the lattice parameter agree very well with the corresponding dependencies of our topological indices. Thus, they constitute a valid characteristic of the system, and in particular, they reveal whether E_{gap} is positive or negative.

(4) In the semimetal Weyl phase, the Weyl's nodes are placed very close in the $\boldsymbol{k}$ space ($\sim$0.02 Å^{-1}), thus the observation of the splitting of Dirac cones using the ARPES technique is not possible at present.

ACKNOWLEDGMENTS

This work was partially supported by National Science Centre NCN (Poland) projects UMO-2016/23/B/ST3/03725 (A.Ł.), UMO-2017/27/B/ST3/02470 (A.Ł.), and UMO-2014/15/B/ST3/03833 (T.S.) as well as by the Foundation for Polish Science through the IRA Programme cofinanced by the European Union within Smart Growth Operational Programme (T.S.).

[1] T. H. Hsieh, H. Lin, J. Liu, W. Duan, A. Bansil, and L. Fu, Nat. Commun. **3**, 982 (2012).
[2] P. Dziawa, B. J. Kowalski, K. Dybko, R. Buczko, A. Szczerbakow, M. Szot, E. Łusakowska, T. Balasubramanian, B. M. Wojek, M. H. Berntsen, O. Tjernberg, and T. Story, Nat. Mater. **11**, 1023 (2012).
[3] Y. Tanaka, Z. Ren, T. Sato, K. Nakayama, S. Souma, T. Takahashi, K. Segawa, and Y. Ando, Nat. Phys. **8**, 800 (2012).
[4] S.-Y. Xu, C. Liu, N. Alidoust, M. Neupane, D. Quian, I. Belopolski, J. D. Denlinger, Y. J. Wang, H. Lin, L. A. Wray, G. Landolt, B. Slomski, J. H. Dil, A. Marcinkova, E. Morosan, Q. Gibson, R. Sankar, F. C. Chou, R. J. Cava, A. Bansil, and M. Z. Hasan, Nat. Commun. **3**, 1192 (2012).
[5] Y. Ando, J. Phys. Soc. Jpn. **82**, 102001 (2013).
[6] S. Safaei, P. Kacman, and R. Buczko, Phys. Rev. B **88**, 045305 (2013).
[7] B. M. Wojek, R. Buczko, S. Safaei, P. Dziawa, B. J. Kowalski, M. H. Berntsen, T. Balasubramanian, M. Leandersson, A. Szczerbakow, P. Kacman, T. Story, and O. Tjernberg, Phys. Rev. B **87**, 115106 (2013).
[8] Y. Okada, M. Serbyn, H. Lin, D. Walkup, W. Zhou, C. Dhital, M. Neupane, S. Xu, Y. J. Wang, R. Sankar, F. Chou, A. Bansil, M. Z. Hasan, S. D. Wilson, L. Fu, and V. Madhavan, Science **341**, 1496 (2013).
[9] K. Dybko, M. Szot, A. Szczerbakow, M. U. Gutowska, T. Zajarniuk, J. Z. Domagala, A. Szewczyk, T. Story, and W. Zawadzki, Phys. Rev. B **96**, 205129 (2017).
[10] Y. Wang, G. Luo, J. Liu, R. Sankar, N.-L. Wang, F. Chou, L. Fu, and Z. Li, Nat. Commun. **8**, 366 (2017).
[11] G. Krizman, B. A. Assaf, T. Phuphachong, G. Bauer, G. Springholz, L. A. de Vaulchier, and Y. Guldner, Phys. Rev. B **98**, 245202 (2018).
[12] A. Łusakowski, P. Bogusławski, and T. Story, Phys. Rev. B **98**, 125203 (2018).
[13] Z. Wang, Q. Liu, J.-W. Luoc, and A. Zunger, Mater. Horiz. **6**, 2124 (2019).
[14] H.-X. Deng, Z.-G. Song, S.-S. Li, S.-H. Wei, and J.-W. Luo, Chin. Phys. Lett. **35**, 057301 (2018)
[15] S. Safaei, M. Galicka, P. Kacman, and R. Buczko, New J. Phys. **17**, 063041 (2015)
[16] X. Gao and M. S. Daw, Phys. Rev. B **77**, 033103 (2008).
[17] M. Geihufe, S. K. Nayak, S. Thomas, M. Dane, G. S. Tripathi, P. Entel, W. Hergert, and A. Ernst, Phys. Rev. B **92**, 235203 (2015).
[18] A. Zunger, S.-H. Wei, L. G. Ferreira, and J. E. Bernard, Phys. Rev. Lett. **65**, 353 (1990).
[19] C.-Z. Chang, J. Zhang, X. Feng, J. Shen, Z. Zhang, M. Guo, K. Li, Y. Ou, P. Wei, L. L. Wang, Z. Q. Ji, Y. Feng, S. Ji, X. Chen, J. Jia, X. Dai, Z. Fang, S. C. Zhang, K. He, Y. Wang, L. Lu, X. C. Ma, and Q. K. Xue, Science **340**, 167 (2013).
[20] Y. Tokura, K. Yasuda, and A. Tsukazaki, Nat. Rev. Phys. **1**, 126 (2019).
[21] J. Liu, C. Fang, and L. Fu, Chin. Phys. B **28**, 047301 (2019).
[22] M. Serbyn and L. Fu, Phys. Rev. B **90**, 035402 (2014).
[23] S. Reja, H. A. Fertig, L. Brey, and S. Zhang, Phys. Rev. B **96**, 201111(R) (2017).
[24] R. Adhikari, V. V. Volobuev, B. Faina, G. Springholz, and A. Bonanni, Phys. Rev. B **100**, 134422 (2019).
[25] T. Story, R. R. Gałązka, R. B. Frankel, and P. A. Wolff, Phys. Rev. Lett. **56**, 777 (1986).
[26] P. J. T. Eggenkamp, H. J. M. Swagten, T. Story, V. I. Litvinov, C. H. W. Swüste, and W. J. M. de Jonge, Phys. Rev. B **51**, 15250 (1995).
[27] P. Lazarczyk, T. Story, M. Arciszewska, and R. R. Galazka, J. Magn. Magn. Mater. **169**, 151 (1997).
[28] G. P. Mazur, K. Dybko, A. Szczerbakow, J. Z. Domagala, A. Kazakov, M. Zgirski, E. Łusakowska, S. Kret, J. Korczak, T. Story, M. Sawicki, and T. Dietl, Phys. Rev. B **100**, 041408(R) (2019).
[29] A. J. Nadolny, J. Sadowski, B. Taliashvili, M. Arciszewska, W. Dobrowolski, V. Domukhovski, E. Łusakowska, A. Mycielski, V. Osinniy, T. Story, K. Świątek, R. R. Gałązka, and R. Diduszko, J. Magn. Magn. Mater. **248**, 134 (2002).
[30] T. Story, C. H. W. Swüste, P. J. T. Eggenkamp, H. J. M. Swagten, and W. J. M. de Jonge, Phys. Rev. Lett. **77**, 2802 (1996).
[31] T. Story, P. J. T. Eggenkamp, C. H. W. Swüste, H. J. M. Swagten, W. J. M. de Jonge, and A. Szczerbakow, Phys. Rev. B **47**, 227 (1993).

[32] A. Łusakowski, P. Bogusławski, and T. Radzyński, Phys. Rev. B **83**, 115206 (2011).
[33] M. Bukała, P. Sankowski, R. Buczko, and P. Kacman, Phys. Rev. B **86**, 085205 (2012).
[34] X. Tan, H. Shao, T. Hu, G. Q. Liu, and S. F. Ren, J. Phys.: Condens. Mater. **27**, 095501 (2015).
[35] G. Tan, F. Shi, S. Hao, H. Chi, T. P. Bailey, Li-Dong Zhao, C. Uher, C. Wolverton, V. P. Dravid, and M. G. Kanatzidis, J. Am. Chem. Soc. **137**, 11507 (2015).
[36] J. He, X. Tan, J. Xu, G. Q. Liu, H. Shao, Y. Fu, and J. Jiang, J. Mater. Chem. A **3**, 19974 (2015).
[37] X. J. Tan, H. Z. Shao, J. He, G. Q. Liu, J. T. Xu, J. Jiang, and H. C. Jiang, Phys. Chem. Chem. Phys. **18**, 7141 (2016).
[38] Y. Liu, S. K. Bose, and J. Kudrnovský, J. Magn. Magn. Mater. **375**, 15 (2015).
[39] See Supplemental Material at http://link.aps.org/supplemental/10.1103/PhysRevB.103.045202 for influence of spatial distribution of cations in the supercell and Hubbard *U*-corrections on the band structures and densities of states.
[40] P. Łazarczyk, M. V. Radchenko, G. V. Lashkarev, T. Story, K. Dybko, and R. R. Gałązka, Semicond. Sci. Technol. **13**, 989 (1998).
[41] G. Bauer, H. Pascher, and W. Zawadzki, Semicond. Sci. Technol. **7**, 703 (1992).
[42] See http://www.openmx-square.org.
[43] D. M. Ceperley and B. J. Alder, Phys. Rev. Lett. **45**, 566 (1980).
[44] M. Cococcioni and S. de Gironcoli, Phys. Rev. B **71**, 035105 (2005).
[45] A. Ciechan, H. Przybylinska, P. Boguslawski, A. Suchocki, A. Grochot, A. Mycielski, P. Skupinski, and K. Grasza, Phys. Rev. B **94**, 165143 (2016).
[46] B. A. Orlowski, S. Mickevičius, B. J. Kowalski, A. J. Nadolny, B. Taliashvili, J. Ghijsen, F. Mirabella, and R. L. Johnson, Surf. Sci. **507–510**, 155 (2002).
[47] S. Miotkowska, E. Dynowska, I. Miotkowski, A. Szczerbakow, B. Witkowska, J. Kachniarz, and W. Paszkowicz, J. Crystal Growth **200**, 483 (1999).
[48] R. J. Iwanowski, W. Paszkowicz, K. Ławniczak-Jabłońska, M. H. Heinonen, B. Witkowska, and J. Feldhaus, Chem. Phys. Lett. **336**, 226 (2001).
[49] E. Prodan, Phys. Rev. B **80**, 125327 (2009).
[50] T. Fukui, Y. Hatsugai, and H. Suzuki, J. Phys. Soc. Jpn. **74**, 1674 (2005).
[51] C.-L. Zhang, T. Liang, N. Ogawa, Y. Kaneko, M. Kriener, T. Nakajima, Y. Taguchi, and Y. Tokura, Phys. Rev. Mater. **4**, 091201(R) (2020).
[52] G. Nimtz and B. Schlicht, *Narrow Gap Semiconductors. Springer Tracts in Modern Physics*, Vol. 98, edited by B. Höhler (Springer-Verlag, Berlin, 1983).
[53] D. R. Khokhlov (ed.), *Lead Chalcogenides: Physics and Applications* (Taylor and Francis, New York, 2003).
[54] J. Niewodniczańska-Zawadzka and A. Szczerbakow, Solid State Commun. **34**, 887 (1980).
[55] T. Liang, S. Kushwaha, J. Kim, Q. Gibson, J. Lin N. Kioussis, R. J. Cava, and N. P. Ong, Sci. Adv. **3**, e1602510 (2017).